Journal of ELECTRONIC MATERIALS, Vol. 47, No. 9, 2018
https://doi.org/10.1007/s11664-018-6452-x


# Dielectric, Hydrophobic Investigation of ABS/$NiFe_2O_4$ Nanocomposites Fabricated by Atomized Spray Assisted and Solution Casted Techniques for Miniaturized Electronic Applications

RAVIPRAKASH MAGISETTY,[1] ANUJ SHUKLA,[2] and BALASUBRAMANIAN KANDASUBRAMANIAN [1,3]

1.—Structural Composite Fabrication Laboratory, Department of Materials Engineering, DIAT(DU), Ministry of Defence, Girinagar, Pune 411025, India. 2.—Defence Laboratory Jodhpur (DLJ), Ministry of Defence, Jodhpur 342011, India. 3.—e-mail: meetkbs@gmail.com

Engineered nanocomposites with tailored dielectric and hydrophobic characteristics are highly desirable for miniaturized electronics. In this context, we have fabricated acrylonitrile butadiene styrene (ABS)/$NiFe_2O_4$ nanocomposites by facile solvent casted and low-volume high-pressure air-atomized (LVHPAA) techniques. The developed nanocomposites consisted of phases such as amorphous ABS, and crystalline nickel–ferrite phases were examined via x-ray diffraction technique. Fourier transform infrared spectroscopic measuration was used to describe ABS polymers, nickel–ferrite oxide constituents, and their interactions. The effect of the space-charge polarization mechanism between particulates and the polymer ($10^1$–$10^2$ Hz and 10–40 wt.%) was analyzed via impedance spectroscopy, which is further augmented by the Maxwell–Wagner Sillars polarization hypothesis. Also, the subsequent oriental relaxation phenomenon ($10^3$–$10^7$ Hz) was analyzed. Moreover, at $\sim 10^7$ Hz for all wt.% (10–40 wt.%), the incremental permittivity attributed oriental resonance phenomena was examined. In addition, the developed nanocomposites DC-conductivity attributed micro/nano-capacitors mechanism, and the AC-conductivity realized reorientational hoping mechanisms were scrutinized. The cole–cole representation of a nanocomposite that explained relaxation oriented insulating characteristics was also elucidated. The hydrophobicity of developed composites was characterized via atomic force microscopy (AFM) and contact angle goniometry. The AFM analysis showed a uniform textured surface morphology with the LVHPAA technique, which renders superior hydrophobic characteristics due to the process induced nano-needle generated roughness factor. The investigation results explain the improvement in the dielectric and hydrophobic characteristics of nanocomposites obtained by the LVHPAA technique. Therefore, these ABS/$NiFe_2O_4$ nanocomposites could be a possible functional material for miniaturized electronic applications.

(Received February 25, 2018; accepted June 14, 2018; published online June 29, 2018)

**Graphical Abstract**

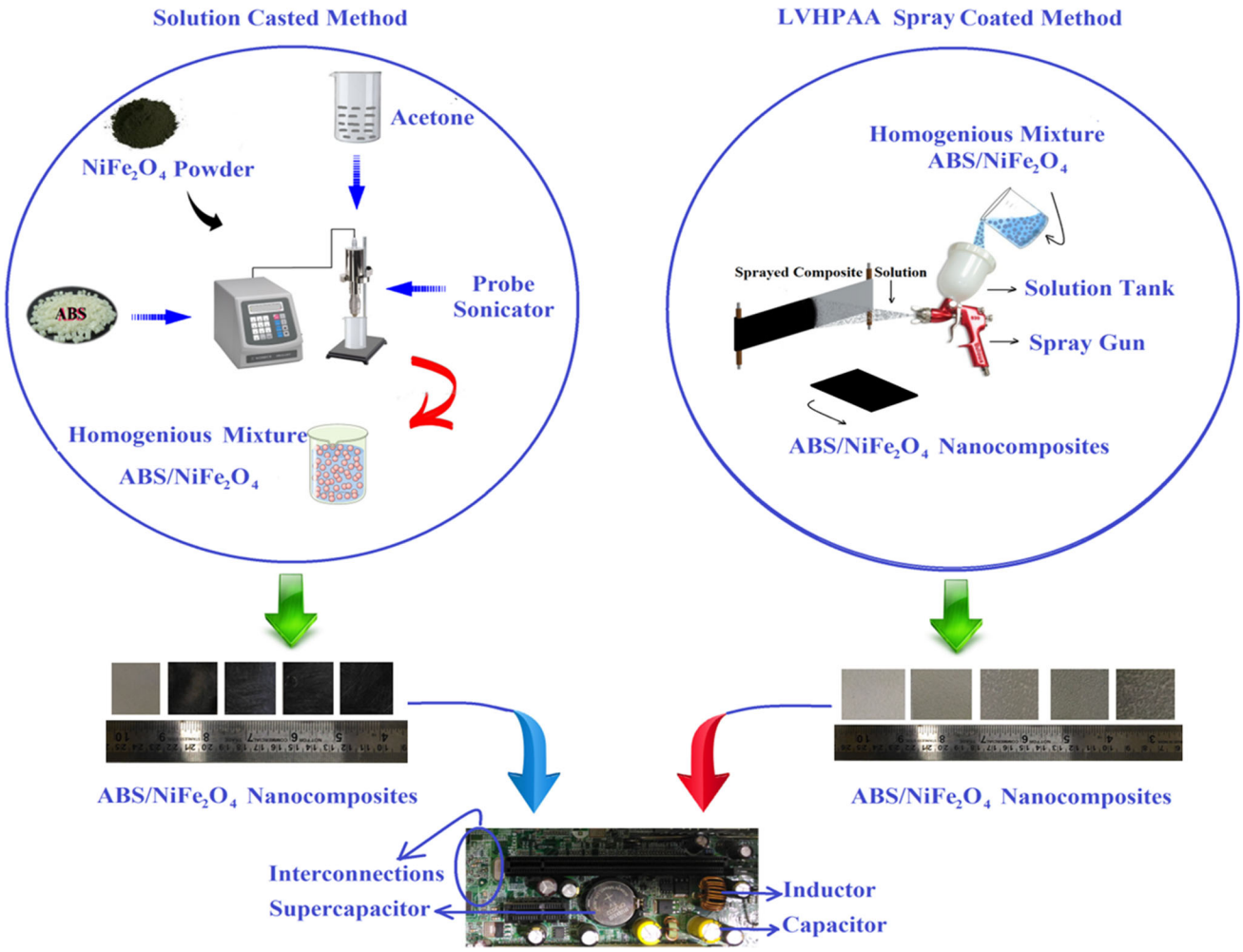


**Key words:** Acrylonitrile butadiene styrene (ABS), NF: nickel ferrite ($NiFe_2O_4$), resonance frequency, Maxwell–Wagners–Sillers (MWS) polarization, conductivity, hydrophobicity

## INTRODUCTION

The entire fundamental electronic packaging system consists of active and passive components, wherein, the passive components such as resistors, inductors, and capacitors can occupy a larger area than the active components. In current wireless communication technology, for example, in cellular mobile devices, the ratio of passive components to the active components is about ~ 20:1. The 80% of circuit board area has been occupying by these discrete passives on an integrated printed circuit board (PCB). Thereby the higher parasitic effects, lower reliability and larger attachment lead to the low performance of electronic devices and their components performance. In many applications interconnected discrete capacitors are extensively utilized for noise suppression, filtering and tuning, decoupling, bypassing, termination and frequency determination, where the discrete capacitor components significantly occupy the larger surface area. Hence, the existing limitations in which capacitors can be placed around the board periphery leads to the device's reduced functionality and results in low performance.[1,2] Moreover, increased fabrication emphasis on efficient electronic packaging may fascinate the demands of passive embedded technology (PET), wherein, the integrated passive components are termed as functional elements which

are incorporated over the substrate surface. In recent years, this passive embedded technology (PET) has been approaching towards miniaturization, which leads to abnormal operating conditions in electronic devices attributed to the miniaturized components inducing stray capacitance effects and additionally insulation failure causes short circuit effects.[3] In order to prevent these abnormalities in electronics, insulating materials with desired dielectric characteristics are dominantly required. However, the moisture absorption may facilitate dielectric breakdown consequently shortening interconnections in-between the electronic parts, simultaneously, instigating a galvanic corrosive effect may decay the overall performance of electronic components. In order to mitigate above all delineated potential problems, insulating characteristics with moisture repellency in nanocomposites are keenly required in wider applications of interconnected miniaturizing electronic technology. In recent days several research groups have investigated exploring materials of low dielectric constant with the hydrophobicity, wherein the researchers have demonstrated a low moisture uptake/hydrophobic feature that was particularly due to the water induced polar groups as a result of dielectric characteristics. This means that the material's moisture phobic characteristics have a synergistic effect on controlling material dielectric characteristics while maintaining water stability.[4,5] Such a type of moisture repellent with dielectric materials is the major concern of materials for a wide range of electronic application fields such as microelectronics, telecommunications, and optical communications.[6–9] Furthermore, researchers have been intensively studying multifunctional hybrid organic, inorganic nanocomposites due to their superior functional, processing advantages as well as that which were utilized as potential large-scale fabrication materials for many technological field applications.[10–12] The carbon nanostructures, semiconducting, metallic and magnetic nanoparticles incorporated in polymer composites have been explored as counter wide-band electronic materials in electromagnetic wave devices to overcome real field abnormal problems.[13–25] In recent days researchers have extensively explored magnetic properties of electrified ferrite incorporated polymer thin films for EMI suppressions and electromagnetic absorber applications due to their electromagnetic wave stimulated functional advantages, wherein the predominant requirement is higher complex dielectric permittivity.[26,27] Simultaneously, considerable efforts have been made in the ferrite thin film fabrication methods, which can induce various merits for wideband electromagnetic wave applications. Wherein, the developments invigorated ferrite thin film fabrication techniques consisting of the plasma-assisted method,[28] chemical vapor deposition (CVD),[29] ferrite plating,[30] sputtering and spin coating,[31,32] spray coating, solution casted, and laser deposition methods.[33,34] Among them, solution casted thin film fabrication technique is considered as an attractive route in terms of cost, process and time, and concurrently, this technique permits fabrication of any shape and thickness without the need of high temperature and other atmospheric conditional requirements.[35–37] However, the electrified ferritic particles are high-density ceramics and produce magnetic fields under applied electromagnetic force fields instigating particle induced agglomerations, which are intensified by their high-density characteristics. Additionally, the inability offered by the magnetic particle dispersion is most likely associated with the clustering effects, which are attributed to interactions between particles as well as a particle and polymer matrix.[38] Therefore, the controlled particle dispersion in thin magnetic polymer composite films has been a challenging technological prerequisite. The alternative synthetic fabrication and processing technique strategies to overcome these intrinsic-steric forces, are simultaneous agglomeration prevention strategies as required. Manish K et al., have reported spray coated technique influenced ferrite thin films are having a greater advantage in EM wave applications, which ascribes to the atomized processing feature rendering particle dispersion interactions under electromagnetic wave to improve device performance.[39] This simple and highly automated industrial spray coated technique consists of a hand controlled industrial air gun pneumatic system, which renders stabilized spraying of nanocomposite fluid flux. Wherein, functional flux is atomized through the spray head nozzle that induces a sequential fluid flux flow from the nozzle. The nozzle induces kinetic impact and controls the droplet size of the composite solution, where the size of the polymer composite droplet is minimized, which provides the composite droplet contained particles that are less consequently sprayed flux droplets containing particles that are prevented from forming a higher number of agglomerations. Therefore, kinetically sprayed composite flux fabricated thin films demonstrate non-agglomerated uniformly dispersed ferrite particles, which has been a motivation to fabricate ferrite thin films by the low volume high-pressure pneumatic fluid flux coated method.

In this present study, we report the practical and straightforward approach to fabricate particulate nanocomposite thin films composed of dispersed $NiFe_2O_4$ particles via the solvent casting method as well as the low volume high-pressure pneumatic fluid flux coated method. Subsequently, the structural characteristics of fabricated particles incorporating polymeric composite thin films were revealed by x-ray diffraction spectroscopy. Simultaneously thin films of acknowledged oxide groups, ABS functional groups, and their interactions have been demonstrated by utilizing FT-IR spectroscopy. Additionally, AFM ascribed roughness factor, and

correlated hydrophobic characteristics were extensively analyzed for the magnetic composite thin films with the aid of AFM and contact goniometry. Moreover, the thin film composite's impedance broadband spectrum analyzer dielectric properties were intellectually elucidated as well as having the dispersion characteristic advantages highlighted.

## MATERIALS AND THIN FILM FABRICATION METHODS

### Materials

Raw materials, ABS (Grade: ABSOLAC-920, melt flow rate 27 g/10 min at 220°C/kg and density = 1.04 g/cc) in the form of cylindrical pellets were procured from Styrolutions ABS India Ltd. $NiFe_2O_4$–nickel ferrite powder (Particle size ∼ 60–170 $\mu$m and Density ∼ 5.13 g/cc) was obtained from Defence Laboratory Jodhpur, Rajasthan, India. Methyl acetate (MW = 74.08 g/mol and Purity = 99.0%) was purchased from Sigma Aldrich Pvt. Ltd., for the preparation of solution casted ABS composite thin films, and LVHPAA spray atomized thin films. All reagents and solvents involved were of analytical grade and were used without any further purification.

### Solution Casted Method of ABS/$NiFe_2O_4$ Thin Film Fabrication

The solution casting method is an entirely primary method to prepare nanocomposite thin films from solution. This thin film fabrication process initiates from dropping of the solution on a flat glass substrate followed by a releasing agent subsequent to the drying process. But, the film forming method, i.e., during the solvent evaporation time, this technique suffers lack of control to produce qualified thin films. Such as a lack of control over thickness and often dispersed high-density particle effects (agglomerations) are observed during the drying process.[34] Additionally, fluid surface tension/surface energy dominates in drying in-homogeneous results with picture forming effects at the corners/edges of nanocomposite films.[34] Simultaneously, inhomogeneous solubility induced polymer precipitation effects dominate during thin film formation.[34] However, Gore et al.[40] have demonstrated the solvent casted thin film nanocomposite fabrication technique is cost-effective and a facile method among the other techniques such as in situ polymerization, melt mixing, melt blending, and the sol–gel method. Therefore, the solvent casted thin film fabrication method has been implemented, consequently, ABS/$NiFe_2O_4$ nanocomposite thin films were obtained. In the typical nanocomposite thin film fabrication process, ABS crystals (2 g) were dissolved in methyl acetate (10 mL) solution using a magnetic stirrer at 400 rpm and 35°C temperature for 1 h. Then the different weight fractioned nano nickel ferrites were added to the ABS dissolved polymer solution (see supplementary Table S1) followed by the ultrasonic probe sonicator (Model No: VCX 750 Sonics and Materials, Inc., CT 06470 USA) operated 30 min at 35°C with 25% energy amplitude for nickel ferrite nanoparticle dispersion in nanocomposite mixture. Consequently, the homogeneous nickel ferrite polymeric composite solution was obtained. Finally, the extracted nanocomposite polymeric solution was used to fabricate nanocomposite thin films on a flat-bottomed glass petri dish (dia $\Phi$ = 100 mm and height $h$ = 10 mm). The thin film fabrication process has been illustrated as shown in Fig. 1.

### Low Volume High-Pressure Air Atomization Method of ABS/$NiFe_2O_4$ Thin Film Fabrication

The sculptured nanocomposite thin films were fabricated by a low volume high-pressure air atomized (LVHPAA) fluid system. This technique is a widely known industrial atomization technique to smear over unified as well as capricious surfaces. Wherein, atomized functional fluid induces uniformed droplet sizes, and uninterrupted droplet flows through the nozzle head, which is illustrated in Fig. 2.[41,42] The pneumatic fluid flux atomized system's nonlinear dominant parameters include surface tension, viscosity, fluid density, air/gas or liquid mass ratio, nozzle diameter, spray speed, droplet size and control over the distance between the nozzle and spray coated substrate that determines the growth of thin films.[43] Among them, air/gas or liquid mass ratio is a preeminent parameter to control the mean droplet size that comprises the minimum number of nanoparticles.[43] In other words, atomized mean droplet size is a critical parametric feature, which enhances nickel ferrite nanoparticle dispersion in nanocomposite thin films.[43] Typically, in an engineered nanocomposite thin film's fabrication process, ABS polymer crystals were dissolved in methyl acetate solution by magnetic stimming action. The resulting dissolved solution was mixed with nickel ferrite nanoparticles (see supplementary Table S1) followed by the sonication for 30 min, then sprayed onto the substrate using apparatus as shown schematically in Fig. 2. The suspension was delivered onto the substrate by an atomized nozzle head, where the atomized droplets by an atomized nozzle were operated with back air pressure at 217.5 psi and the fluid flux rate at 2 mL/min. The distance between the substrate and the nozzle was fixed at 15 cm for uniform distribution. The atomized droplets form a fine solvent mist on the substrate that was avoided at 40°C in a furnace.

As fabricated nanocomposite thin film thickness was obtained by digital thickness gauge, where the casted technique nanocomposite mean thickness value was ∼ 0.45 mm, and low volume high-pressure air atomized (LVHPAA) spray coated thin film technique nanocomposite mean thickness value at about ∼ 0.45 mm was observed.

### Characterization Techniques

As fabricated composite thin films were collected to carry out different characterization studies,

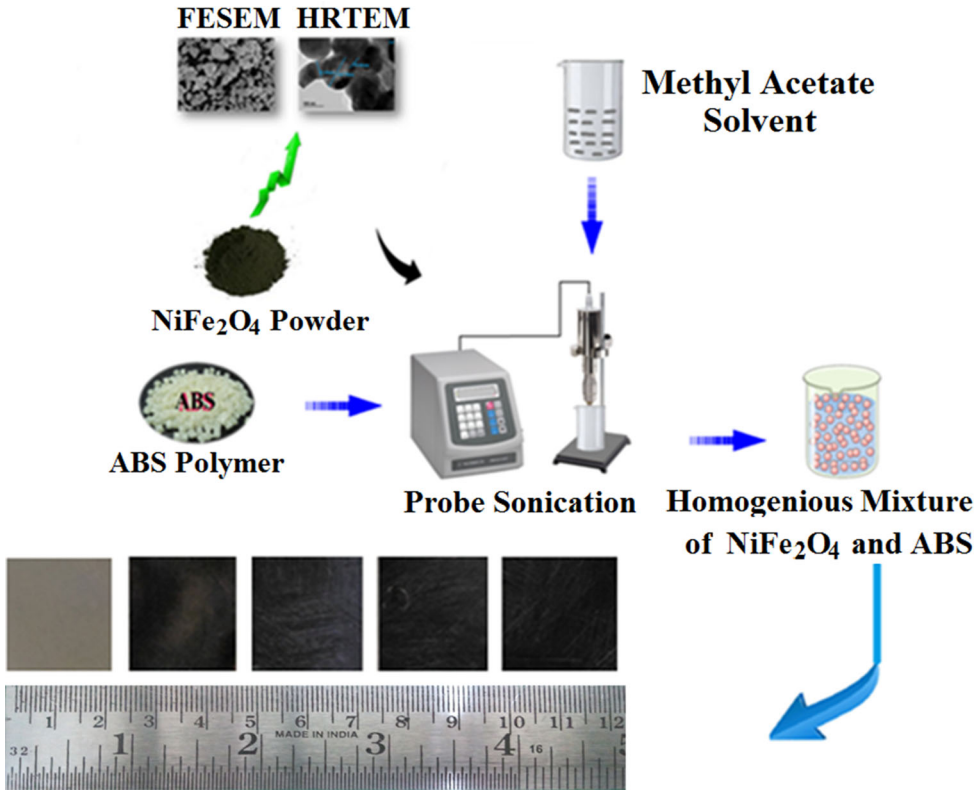


Fig. 1. Preparation of nanocomposite thin films via solution processed technique.

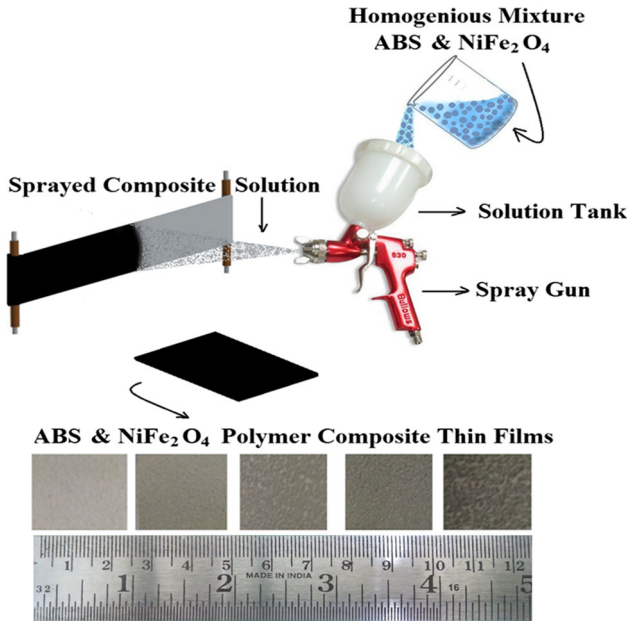


Fig. 2. Preparation of nanocomposite thin films via low volume high pressure air atomized (LVHPAA) spray coated technique.

include thin film composite x-ray diffraction spectroscopy (XRD), this investigation was effectuated with the aid of Bruker - x-ray diffraction spectroscopy, USA. Additionally, ABS/$NiFe_2O_4$ thin film's Fourier transform infrared (FTIR) spectroscopic functional groups were examined by utilizing BX-FTIR Spectroscopy (Perkin Elmer Inc., USA) at ambient temperature (3500–500 $cm^{-1}$). Moreover, the room temperature dielectric properties were scrutinized as per ASTM D150 standard within the frequency range 1–10 MHz by utilizing broadband impedance spectroscopy (Nova-control—ALPHA, Germany). Furthermore, surface topographic roughness measuration was performed for thin film nanocomposites by atomic force microscopy (AFM-Metris 2001A NC, Burleigh Instruments, Inc.). Subsequently, the static water contact angle was measured with the aid of a contact angle goniometer (DSA-100, Kruss GmbH, Germany) using deionized water at room temperature, where the droplet volume 8 $\mu$l was maintained. The contact angle was evaluated after balancing fundamental steric forces in the injected droplet; an average of five measurements was made to analyze thin film's wettability behavior. Simultaneously, these goniometric contact measurements were correlated with the AFM examined topographic roughness to elucidate thin film hydrophobic characteristics.

## Structural Analysis

X-ray diffraction patterns representing structural information of nanocomposites is illustrated in Fig. 3. In course, the XRD pattern at $2\theta$ = 15°–25° demonstrates successive confirmatory area under

the peak pertinent to the amorphous nature of the ABS polymer, which is highest for pristine ABS thin film and is consistent with results obtained by Vinay et al.[44] Subsequent high intense peaks at $2\theta$ correspond to the Miller indices ($hkl$) attributed to the nickel ferrite phase, and this was confirmed by JCPDS data (see supplementary Table S2). Whereas, in an ABS XRD peak with conjugated scaling area, this disappears while increasing the nickel ferrite phase in thin films, which is attributed to the enforced chain alignment due to accommodated crystalline particles; and, as a result, the amorphous nature of ABS polymer is approaching towards crystallinity.[26,44] Moreover, the FWHM of a 10 wt.% intense (311) peak indicates a small increase in crystallinity.[45] In contrast to the ABS, the nanocomposite thin films crystallinity was increased markedly, which probably can be attributed to the higher nickel ferrite concentrations.[45] The higher the concentration of nickel ferrites in thin film, the more intense these emergent nanocomposite peaks are, although the peak width is similar. The nickel nanoparticles might act as nucleation sites for nanocomposite crystalline structure growth. Hence, the nanocomposite thin films with a higher wt.% of nickel ferrites showed a considerable crystalline intensity. Whereas, Vinay Panwar et al., have demonstrated the improper crystalline filler dispersion or inappropriate bonding between filler surface and amorphous polymer chain renders a disordered structure; consequently, the reduced composite crystallinity was obtained.[44] This feature was improved in nanocomposite thin films and is illustrated in Fig. 3, and which was probably due to thin film composites as elucidated in interfacial bonding between polymer and filler particulates.[26] Moreover, this can be further augmented with the aid of FT-IR spectroscopic characterization spectra.

The regular interfacial interaction between ABS and nickel ferrite in nanocomposite thin films has been confirmed via FTIR spectroscopic technique as illustrated in Fig. 4. The essential vibrational absorption peaks and their corresponding structural features were elucidated (see supplementary Table S3).[46] Wherein, nickel ferrites M–O interaction wave numbers ranging from 700 $cm^{-1}$ to 490 $cm^{-1}$ are attributed to the absorption of interfacial infrared wave energy through metal–oxygen vibrational stretching interactions between tetrahedral and octahedral groups, respectively.[26] The peak located at 2237 $cm^{-1}$ is attributable to a CN bond, which corresponds to the acrylonitrile monomer. The other subsequent bonds belong to the aromatic ring of the styrene component, which has been located at 1610 $cm^{-1}$, 1470 $cm^{-1}$, 760 $cm^{-1}$ and 699 $cm^{-1}$ with the butadiene monomer bond corresponding to band nearer 1005 $cm^{-1}$ and the bond appeared at 911 $cm^{-1}$ which is also belongs to butadiene monomer.[40,47,48] The simultaneous appearance of peaks located at 3301 $cm^{-1}$, 1637 $cm^{-1}$ and 1552 $cm^{-1}$ is attributed to that of noncyclic N-monosubstituted amide, which may arise from the toughening and antistatic additives to the ABS by manufacturers.[49] The appearances of additive induced peaks are consistent with the obtained FT-IR spectra. Moreover, the absorbance of the peak located at 1637 $cm^{-1}$ is attributed to overlapped ABS C=C stretch mode with the C=O stretch mode of the amide. Additionally, a bond located at 1735 $cm^{-1}$ in thin films was observed, which is ascribed to the ether group carbonyl stretch mode. Further, it can be attributed to that of the existing additive in ABS formulation, i.e.,

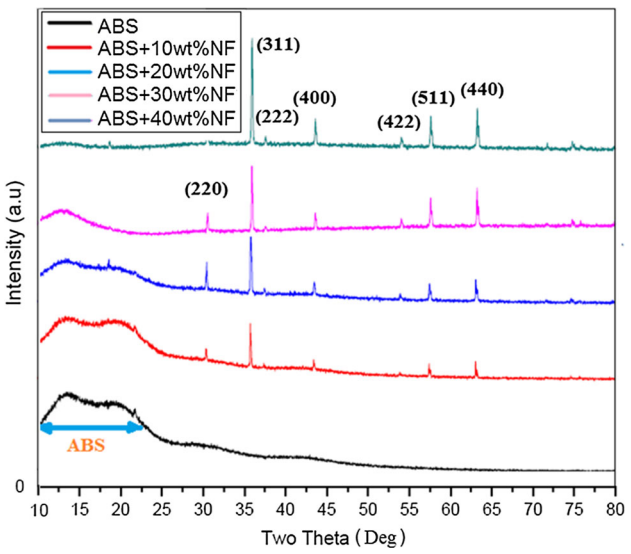


Fig. 3. X-ray spectroscopic characteristic spectra of polymer composite (ABS and ABS/$NiFe_2O_4$) thin films.

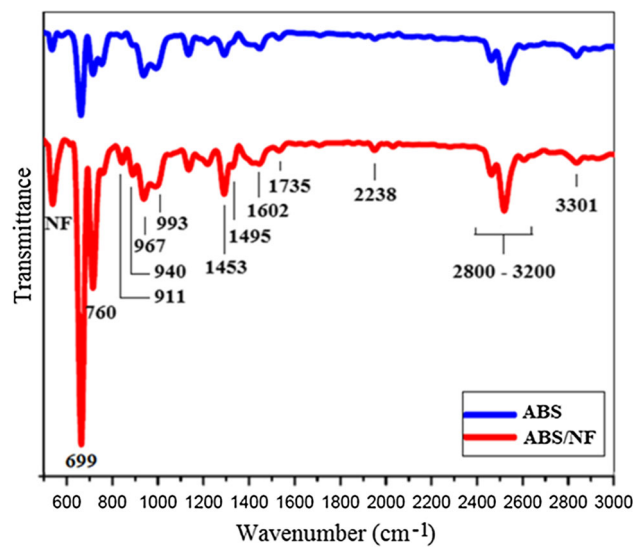


Fig. 4. FT-IR characteristic spectra analysis of nanocomposite thin film.

probably a hindered amine light stabilizer (HALS)[49] or phenolic antioxidant (PA)[50,51] Whereas, in ABS/$NiFe_2O_4$, there are some specific bands (wave numbers) demonstrating nickel ferrite phase, and the subsequent absorption bands (wave numbers) corresponding to the ABS polymer phase. Which probably elucidates an ABS polymer that is well wrapped over nickel ferrite nanoparticles. Additionally, the observed thin films characteristic absorption peaks are slightly moved from their original position, which probably can be attributed to that of bond stretching and bending strategies[40]

## Dielectric and Conductivity Analysis

Room temperature frequency dependent characteristics (10–10 MHz) of as fabricated (solution casted and LVHPAA spray coated) thin films were investigated as per the ASTM D150 with the aid of utilizing an impedance Nova control dielectric spectroscopy analyzer (Novacontrol, Alpha-A, Germany). Wherein, the sample dimensions were cautiously maintained to that of brass circular capacitor plates (ø 20 mm), then loaded into a brass electrode dielectric cell. The frequency (10–10 MHz) dependent characteristic capacitance was obtained, the obtained dielectric permittivity '$\varepsilon$' can be attributed according to the mathematical formula as given in Eq. 1.

$$C = \frac{\varepsilon_0 \varepsilon_r A}{d}, \tag{1}$$

where $C$ = measured capacitance, $A$ = area of the electrode plate, $d$ = thickness of a medium, $\varepsilon_0 = 8.85 \times 10^{-12}$ F/m = permittivity of free space and $\varepsilon_r$ = permittivity of the medium, respectively. However, the dielectric constant is equivalent to the relative permittivity or the absolute permittivity of the medium.[52,53] This can be described as a complex mathematical form and is expressed as $\varepsilon^* = \varepsilon' + i\varepsilon''$, where, $\varepsilon'$ = real part of the permittivity, which attributes to the measure of how much energy is stored in applied external force fields. Likewise $\varepsilon''$ = imaginary part of the permittivity, which is attributed to the loss or dissipative nature of a material to an external source and $i = (-1)^{\frac{1}{2}}$.[52,53] Moreover, this deterministic complex permittivity conceptual characteristics can be explained with the aid of vector representation, known as a tangent loss vector diagram. Wherein, the dielectric constant $\varepsilon'$ and dielectric loss $\varepsilon''$ can be calculated from measured capacitance data '$C$', those mathematical expressions are given in Eqs. 2 and 3.[52–54]

$$\varepsilon' = \frac{C'd}{A\varepsilon_0}; \tag{2}$$

$$\varepsilon'' = \varepsilon' \tan\delta \tag{3}$$

Furthermore, the AC conductivity $\sigma_{AC}$ can be calculated according to the Universal Jonchser Power Law relation as represented in Eq. 4.

$$\sigma_{AC} = \varepsilon_0 \omega \varepsilon' \tan\,\delta, \tag{4}$$

where $\omega$ = angular frequency.[52–55] Additionally, the complex impedance can be represented as $Z^* = Z' + iZ''$ where $Z'$ = real impedance and $Z''$ = imaginary impedance.[56]

The frequency respective dielectric constant $\varepsilon'$ characteristics attributes of LVHPAA spray coated and solution processed ABS + $NiFe_2O_4$ thin films with varying concentration is elucidated in Fig. 5a and b. The fabricated pristine ABS polymer thin film demonstrates constant dielectric permittivity characteristics, and simultaneously exhibits ~ zero slope within the frequency range (100–1 MHz). Such a demonstrated result in pristine ABS and ABS nanocomposite's permittivity characteristics can be attributed to their intrinsic oriented dipole oscillations under the vicinity of applied alternating electric fields, and the oriental resonance phenomena governing the frequency dependence.[57] The material influenced by applied alternating electric fields produces resonance at the resonance frequency, which in turn causes higher dipole oscillations and consequently higher dielectric permittivity at the resonance frequency. This phenomenon was observed from $10^{-7}$ s in Fig. 5a and b, of the as-fabricated nanocomposite thin films by LVHPAA spray atomized and solution casted methods. If the applied frequency is higher than that of resonance frequencies, the polarization of polymer dipoles cannot keep up with the applied alternating frequencies. Hence, the polarization mechanism vanishes and contributes to a decaying polarization response of dielectric as seen by Maex et al.[58] Wherein, the inherent delay of orientation dipoles takes time to align within the enforced field, as delay increases and consequently the orientation polarization mechanism vanishes. Typical orientation polarization relaxation/delay times are within the range of $10^{-1}$–$10^{-9}$ s, which can demonstrate a resonance frequency range of that polarization mechanism, this characteristic feature was observed in Fig. 5a and b. Moreover, the ABS nanocomposites with different nickel ferrite weight fractions demonstrated dielectric permittivity increases with increasing fractions, which is probably an attribute of higher oriented dipole concentration at higher nickel ferrite weight percent (see supplementary Table S1). This dielectric delineation was superior in the case of nanocomposites obtained by the LVHPAA spray technique, which has been embellished in Fig. 5b and (see supplementary Table S1). The superiority in dielectric characteristics by the LVHPAA assisted technique

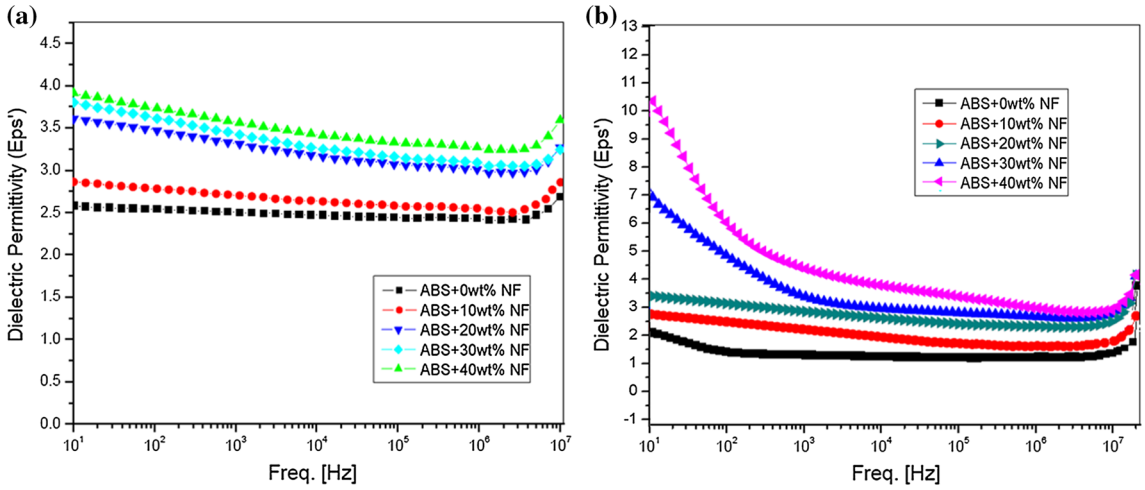


Fig. 5. Variation of dielectric constant versus frequency of thin film polymer ABS and (ABS + $NiFe_2O_4$) composites. (a) Solution casted thin films, and (b) LVHPAA spray coated thin films.

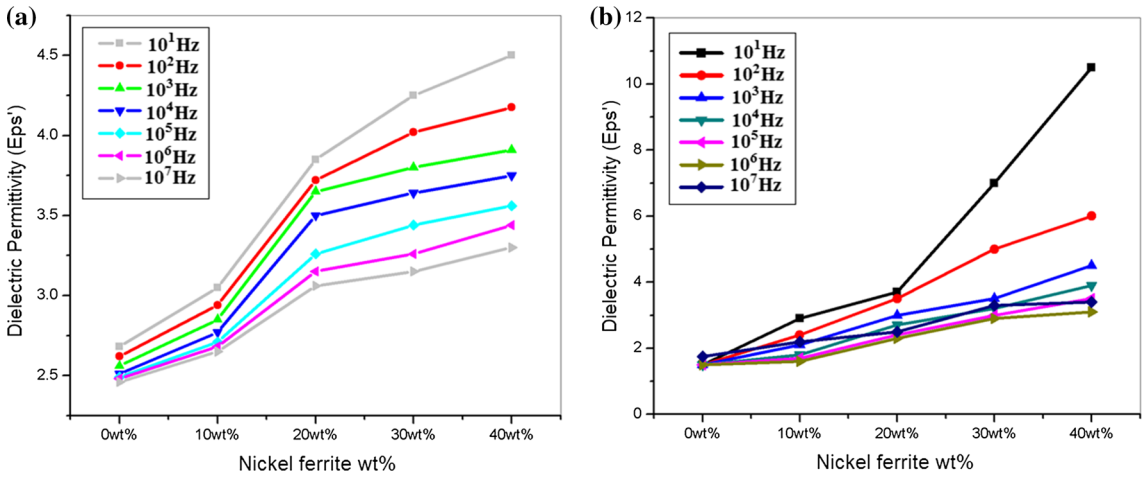


Fig. 6. Variation of dielectric constant with respect to wt (%) of $NiFe_2O_4$ in composite at different frequencies. (a) Solution casted thin films, and (b) LVHPAA spray coated thin films.

was majorly attributed to atomized dispersion with particles encapsulated by ABS polymer. Furthermore, it is also evident that the dielectric constant characteristic slope at a lower frequency region is larger than a higher frequency region, which can be additionally treated as the more significant difference in dielectric constant at lower frequencies than higher frequencies. Since the $NiFe_2O_4$ is a ceramic, it may generate space charges at interfaces, between the particle and ABS polymer segments, which are preeminently active at lower frequencies than higher frequencies and thus the deterministic larger dielectric permittivity. This can be extensively elucidated with the aid of the MWS interfacial polarization mechanism.[52,59,60] Where, the higher value of interface area to volume ratio intensifies their interaction with ABS polymer under the application of the alternating field, which is significantly attributed to the space charge interactions or short range dipoles interactions at the interfaces of particle and insulating ABS material and consequently the considerable polarization effect. At lower frequencies, these space charge dipoles are much more responsive to an applied alternating field, hence increasing dielectric constant values at lower frequencies is observed in Figs. 5 and 6. However, as-fabricated nanocomposites obtained by the LVHPAA (Fig. 5b) technique illustrates the lowest damping decrement in its lower frequency dielectric characteristics as due to the polymer encapsulated particles, whereas 40 and 30 wt.% samples are more prominently elucidated by higher dielectric values correlating with thin films obtained by the solvent casted technique. Moreover, the characteristic curves represent minimum slope characteristics rather than sudden stepwise phenomena at lower frequencies, which are possibly due to the reduced interfacial air gaps

in between polymer and filler material during film fabrication process.[61,62] It also reveals that the dielectric characteristic values were increasing with the addition of filler content in nanocomposite thin films. Additionally, this suggests that in ABS + $NiFe_2O_4$ composite thin films, the nickel ferrite particles act as intermediate in-between segments of amorphous chains and which can penetrate through the molecular bundle of ABS polymer rendering the existence of chain elongation, which might be the one of the reasons for the incrementing nature of the dielectric constant of as-fabricated nanocomposites by the LVHPAA technique (Fig. 5b).[63]

In general, several factors are contributing to dielectric losses in nanocomposite films; they are MWS dipole relaxation/reorientation and residual leakage current/conduction current. In ABS and ABS/$NiFe_2O_4$ composite thin films, losses are associated with $NiFe_2O_4$ as well as the ABS polymer phases, where the moisture-induced interfacial air gaps are the primary aspect of gaining losses, reorientation and residual leakage current/conduction current. As fabricated thin film's frequency dependent (10–1 MHz) dielectric loss tangent (tan $\delta$) characteristics are elucidated in Fig. 7a and b. Wherein, for Fig. 7a the increasing trend in losses with the frequency (10–10 MHz) as well as with the nickel ferrite weight percent from 10 Hz to 1 kHz is probably attributed to a conduction mechanism, dipole relaxation mechanism or the non-homogeneous thickness of thin films.[64,65] However, the conduction mechanism can be ascribed due to direct contact between ferrite particles, where is present the electron jumping known as hopping charge carriers, that is a basic loss mechanism at near relaxation frequencies, consequently, at higher tan $\delta$, which increases with increasing $NiFe_2O_4$ wt.%. Additionally, loss characteristics represent a stepwise tan $\delta$ increment from $10^5$–$10^7$ and attributable to the resonance frequency of that polarization, this causes the maximum alignment of dipoles at resonance frequency with applied alternating field to generate dipole losses that could be a reason for represented loss characteristics in Fig. 7a.[60–62,66,67] Moreover, these can be attributed to a nickel ferrite structural mismatch with polymer phase.[68] Additionally, the structural mismatch probably induces localized space charges and consequently Maxwell–Wagner Sillar interfaces, thereby obtaining the loss tangent.[69,70] Furthermore, ferrites have electronic exchange between trivalent and divalent Fe-cations, which is accompanied by ferromagnetic resonance (FMR) phenomena, hence, beyond certain critical frequencies, losses monotonically decrease with increasing frequencies. Additionally, this can be elucidated by domain wall motion, a relaxation mechanism associated with loss component induced polymer phase,[71] which has been demonstrated in LVHPAA spray coated thin film characteristics as shown in Fig. 7b, meanwhile the other peaks suggest stepwise relaxation is a Debye-type.[31] Furthermore, in Fig. 7b, the dielectric loss mechanism illustrates a culminating nature and slight maxima shift, it is also noted that the peak decreases with increasing frequency. This attribute is according to the relation $\omega\tau = 1$, where $\omega$ is the angular frequency $\omega = 2\pi f$ and $\tau$ is the relaxation time. The '$\tau$' relates the jumping polarization probability per unit time $\tau = \frac{1}{2p_t}$ and is directly proportional to the frequency $\tau = \frac{1}{2p_t} = \frac{1}{f}$, i.e., $f \propto p_t$, hence, the maxima can be observed. However, the peak magnitude is higher in a 20 wt.% sample with the frequency ranging from 10 Hz to 10 MHz, which was probably the secondary peak, this has been illustrated in Fig. 7. Whereas, the peak magnitude shifts from higher

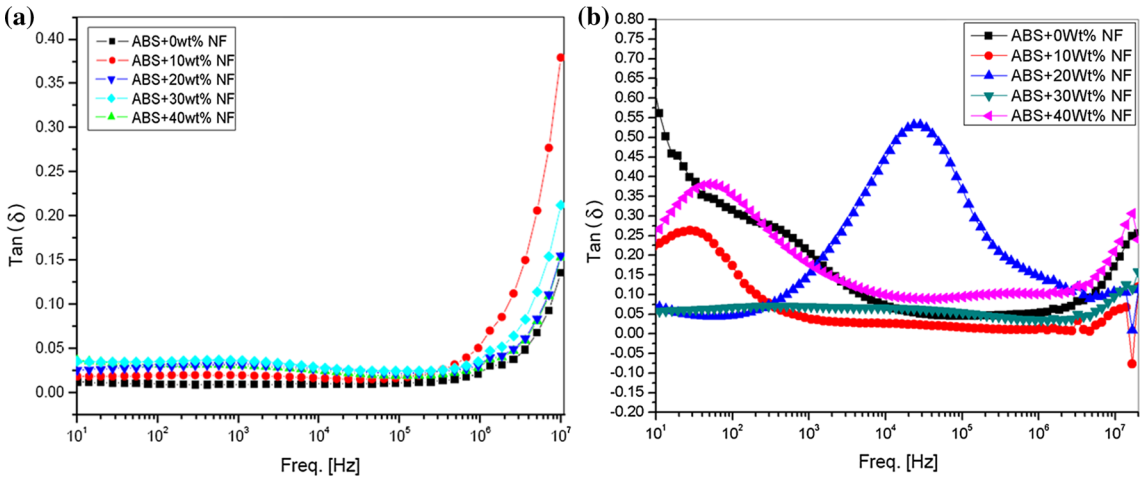


Fig. 7. Variation of dielectric loss versus frequency of ABS and (ABS + $NiFe_2O_4$) composites. (a) Solution casted thin films, and (b) LVHPAA spray coated thin films.

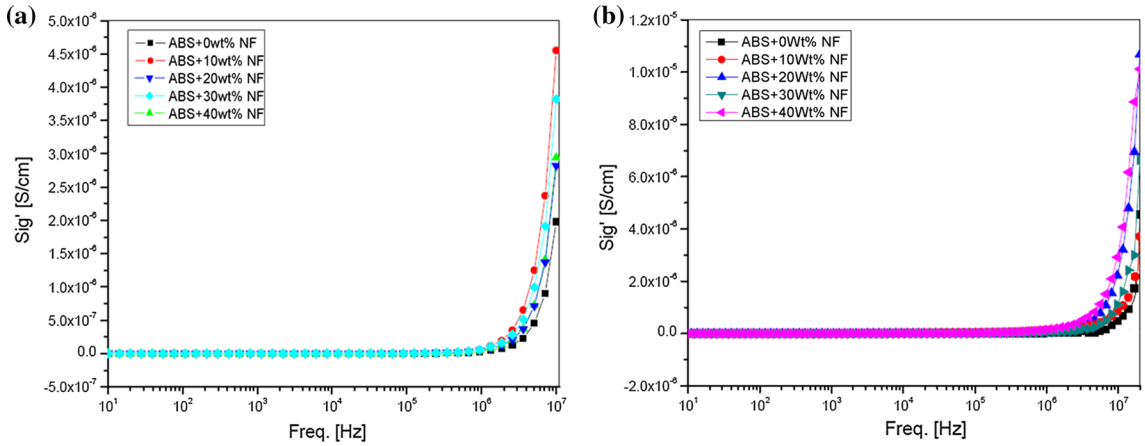


Fig. 8. Variation of conductivity versus frequency of ABS and (ABS + $NiFe_2O_4$) composites. (a) Solution casted thin films, and (b) LVHPAA spray coated thin films.

magnitude peaks to the lower magnitude peaks while increasing frequencies are concerning different wt.% and can be attributable to the actively participated electronic exchange polarization mechanism between $Fe^{2+}$ and $Fe^{3+}$.[27]

Thin film polymer composites AC conductivity is attributed to the type of triggered electronic charge transport mechanism, which is governed by the material intrinsic characteristics. The frequency dependent conductivity of pristine ABS and ABS/$NiFe_2O_4$ thin films with varying concentration of $NiFe_2O_4$ has been elucidated in Fig. 8a and b, respectively. The obtained frequency dependent conductive characteristic composite thin film logarithmic illustration has elucidated a plateau region at the lower frequency and further augmented as per frequency, which can be interpreted by the Universal Jonscher's Power Law (JBL) hypothesis as exemplified in Eq. 4.[54,55] However, the fabricated composite thin films with varying weight fractions of $NiFe_2O_4$ involve two regions of frequency, i.e., at lower frequency range $10^{-1}$–$10^7$ Hz and the higher frequency range $10^5$–$10^7$ Hz.[54,55] Wherein, the DC conductivity is dominated by the lower frequency region, which primarily is attributed to the dipoles existing in air gap interfaces between the ABS polymer and nickel ferrite particles in the interfacial polarization mechanism. Additionally, this can be elucidated with the aid of the micro/nano-capacitor principle, where the static electronic exchange takes place in interfacial air gaps as a result zero conductivity.[62] Moreover, at higher frequencies, $10^5$–$10^7$ Hz. , the conductivity hypothesis follows frequency dependent characteristics that can be extensively elucidated by the Maxwell–Wagner Sillars (MWS) interfacial polarization mechanism and the dielectric relaxation mechanism.[56] Furthermore, the momentum of mobile charge carriers in the reorientational hopping mechanism deals frequency dependent conductivity at higher frequency ranges, wherein the electron hopping probability across the reorientational dipolar chain facilitates the conducting route through the amorphous zone of polymer drives towards the incremental increase in conductivity.[54,55,72] This might be the one of the reasons in the enhancement of conductivity while increasing weight concentrations, which is more prominent in nanocomposites fabricated by LVHPAA technique than by the solvent casted technique (Fig. 8a and b). However, the solution casted thin film 20 wt.% nanocomposite elucidates higher conductivity compared to the other thin films, which is attributed to the electron driving force enabled mobile charge carrier, as well as the magnetically coupled nickel ferrite agglomerations, and provides the path for electrons participating in the enhancement of conductivity at higher frequencies, as a result, the conductivity is $4.5 \times 10^{-6}$ s $cm^{-1}$ as compared to the pristine ABS $2.0 \times 10^6$ s $cm^{-1}$ Likewise, LVHPAA spray coated samples are revealed at the higher frequency $10^5$–$10^7$ Hz region, the conductivity is increasing while increasing the nickel ferrite concentrations, which can be attributed by the nickel ferrite encapsulated ABS polymer phase that induces an interconnected network providing the path for the flow of mobile charge carriers by the arbitrarily moving electrons.[73]

Complex impedance spectroscopic investigation is a well-known technique to examine dielectric material properties,[56] additionally, which can resolve various contributions such as electrode effects, bulk effects, and their interfaces. The imaginary versus real impedance (*Z″Versus Z′*) plot elucidates dominant resistance and is insensitive to smaller resistances, which is the reason for losses in nanocomposites, where the losses by the LVHPAA spray coated method is superior, this has been illustrated in Fig. 7a and b.[74] Moreover, the ideal cole–cole characteristics (*Z″Versus Z′*) are semicircles.[31] Whereas, as fabricated thin film's cole–cole characteristics are producing linear representations

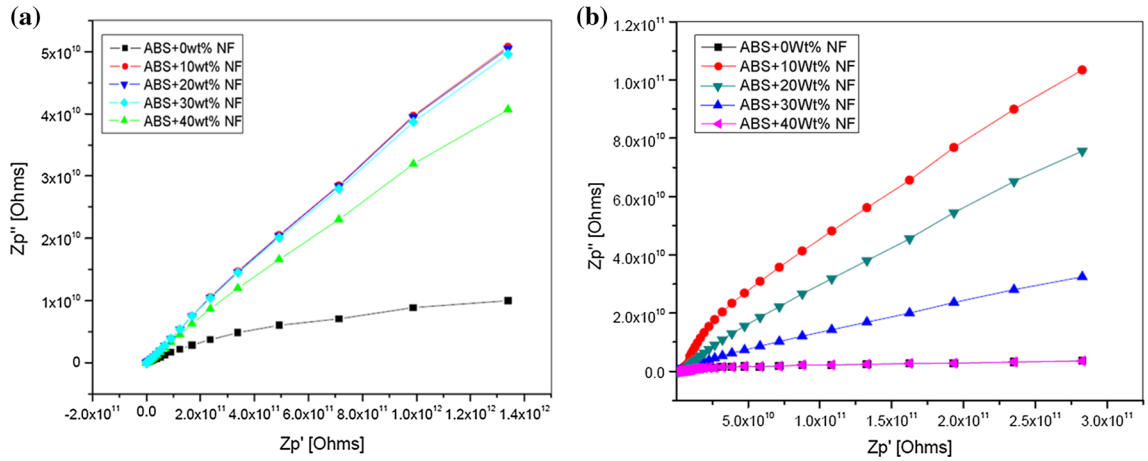


Fig. 9. Cole-Cole plots for ABS and (ABS + $NiFe_2O_4$) composites. (a) Solution casted thin films, and (b) LVHPAA spray coated thin films.

(10 Hz to 10 MHz), which is illustrated in Fig. 9a and b. This probably is attributed to the room temperature respective hypothesis.[31] Simultaneously, the center of semicircular characteristic curves in Fig. 9a and b, are existing outside of the real impedance axis, which is attributed to the distributed passive elements (resistance, capacitance and inductance) in thin films to that of electrodes in a real system. These passive elements are the predominant elements participating in a relaxation mechanism and consequently relaxation time '$\tau$', which is in good agreement with the loss tangent concept explained above in relation to illustrate Fig. 7a, b. The relaxation time is the time taken by a particular polarization mechanism to occur in dielectric thin films, which was observed higher in LVHPAA spray assisted nanocomposites, where the space charge polarization mechanism ($< 10^{-2}$ s) to oriental/dipole polarization mechanism ($10^{-2} - 10^{-7}$ s) over the frequency range was observed, thus the cole–cole characteristic curves were faintly illustrating two semicircular projections' integrated linear characteristics. However, the relaxation time '$\tau$' is not a discrete quantity, it varies with respect to the mean value. The angle at which these dispersed semicircles is related to the distribution of relaxation time in a polarization mechanism, where the frequency inversion to the imaginary impedance value reveals the relaxation time and the intercept indicates the resistance of the material. The radius of these arcs is increasing with different wt.% from pristine thin film, where the LVHPAA spray administered samples are elucidating higher relaxation time and higher resistances, hence, the higher dielectric characteristics and simultaneous resistance induced higher losses were observed. It can be seen that in reported cole–cole plots of the composition, as shown, two interconnected semicircles correspond to the thin films, which is indicating the appearance of one more interconnected semicircles at lower frequencies and the second semicircle might be at higher frequencies to elucidate the frequency-dependent polarization mechanism existing in nanocomposites.[31,56,71]

## Surface Textured Hydrophobic Analysis

Small size, high speed, low power and low-cost electrostatic actuators have provided significant advantages over thermal devices by minimizing power consumption, by reducing size and less power consumption over electromagnetic devices and by providing faster responses than the piezoelectric devices in many applications, such as electrical and magnetic scaling, MEMS, optical networks and wavelength division multiplex (WDM) systems.[75–77] However, the isolated electrodes in electrostatic actuators reduce its sensitivity to the environmental humidity as well as touch mode electrostatic actuators incurring abnormal operations for their use in outdoor and in many unprotected humid environments.[75] Therefore, in such conditions hydrophobic materials are intended to be both electrically isolating and chemically stable under intended humid environments, which can be accomplished by hydrophobic coating on the surfaces of dielectrics with the hydrophobic layer or the usage of conjugated intrinsically induced hydrophobicity in dielectric composites so that water will not be absorbed on the surface.[75] The absorption of water forms a continuous conducting layer, which produces relatively high surface conductivity and reduces the square wave AC voltage, consequently reducing sensitivity. This can be prevented with the aid of a hydrophobic coating, which induces the droplets on the surface from the condensed water where the hindering effect of leakage current enhances the electrostatic actuation up to the stabilized material hydrophobicity.[75] Moreover, hydrophobic insulating materials are extensively utilized in high voltage applications, where the improved hydrophobicity induces suppressing of

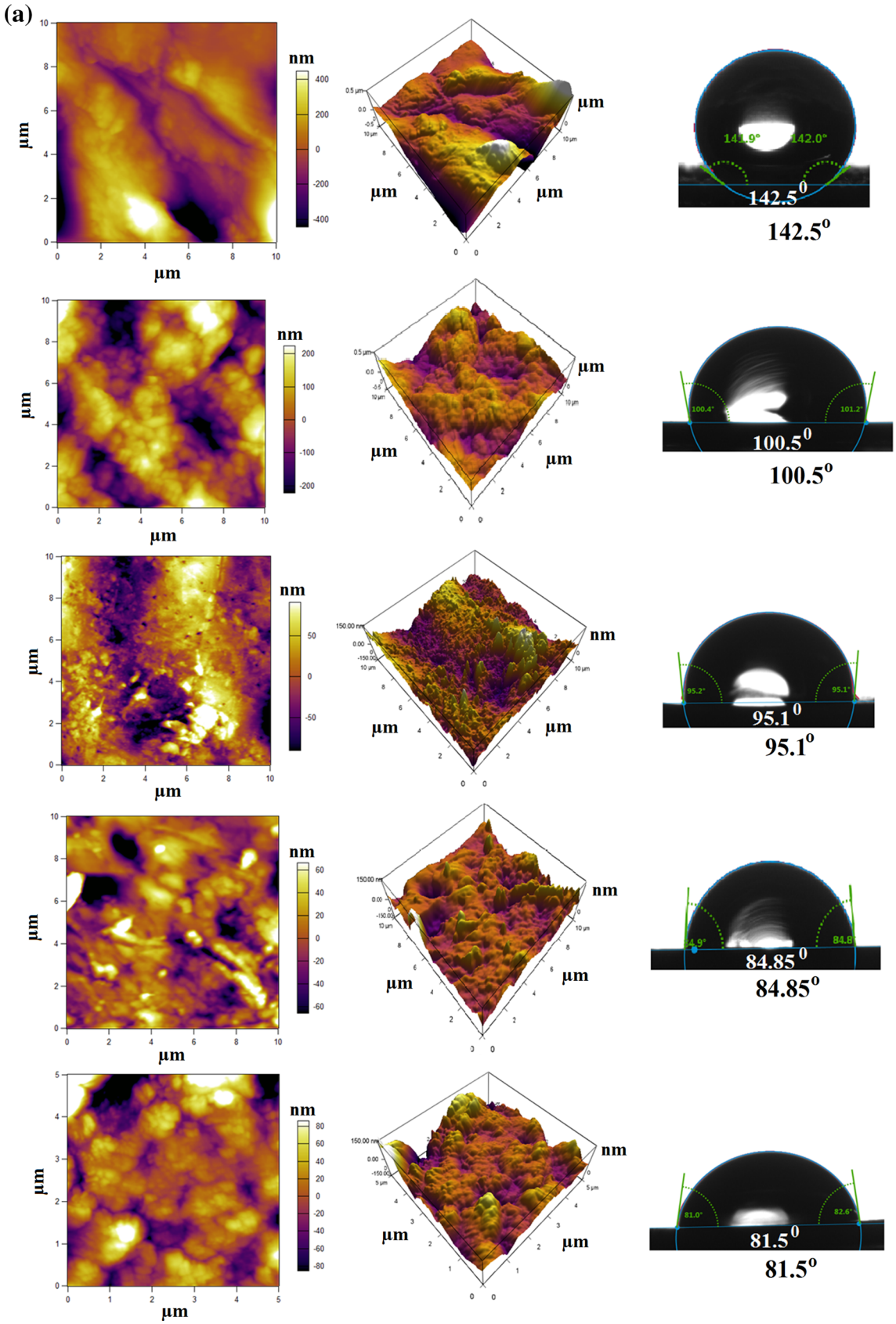


Fig. 10. Atomic force microscopy topographical roughness characteristics at different $NiFe_2O_4$ weight fractions. (a) Solution casted thin films, and (b) LVHPAA spray coated thin films.

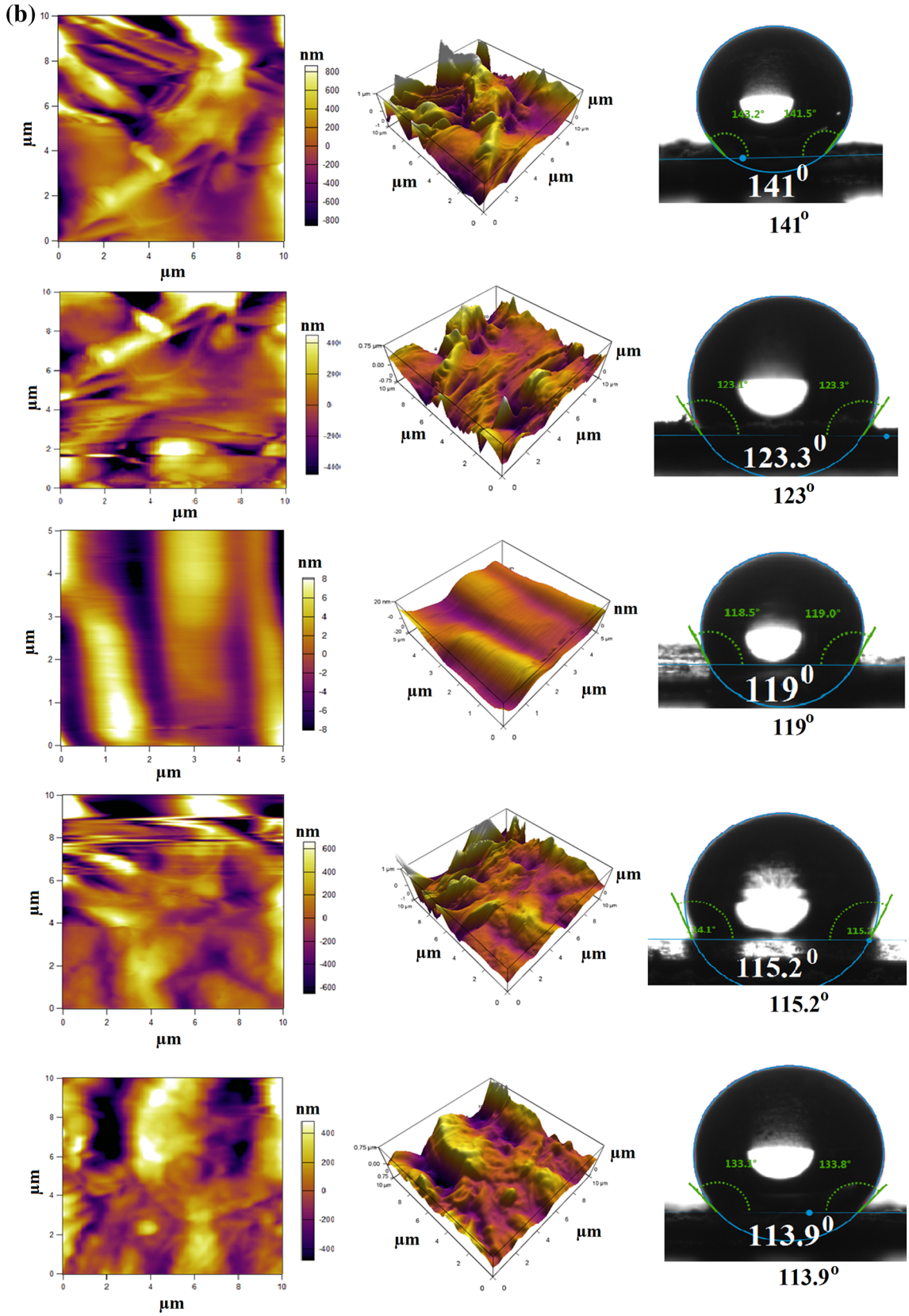


Fig. 10. continued.

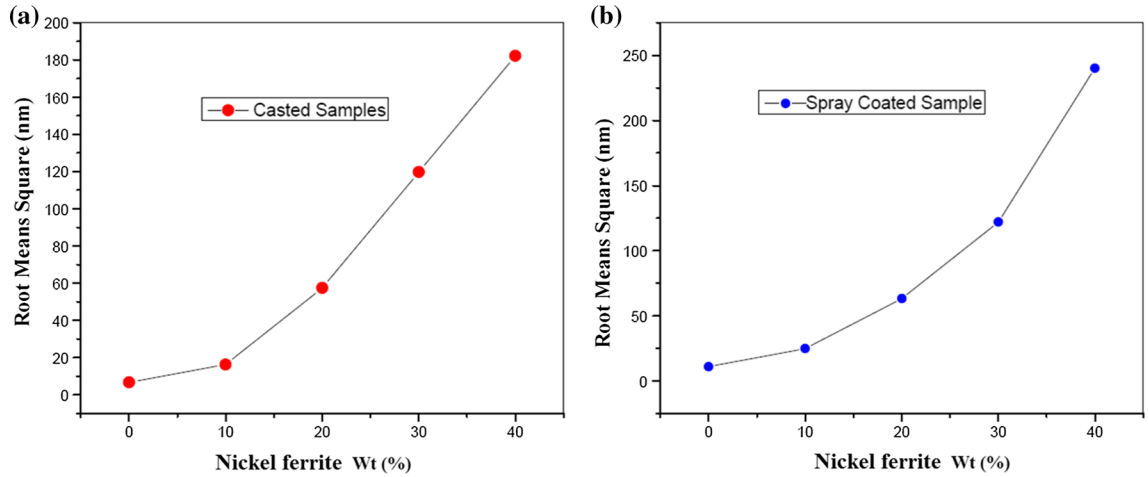


Fig. 11. Linear nanoscale roughness characteristics values at different $NiFe_2O_4$ weight fractions. (a) Solution casted thin films, and (b) LVHPAA spray coated thin films.

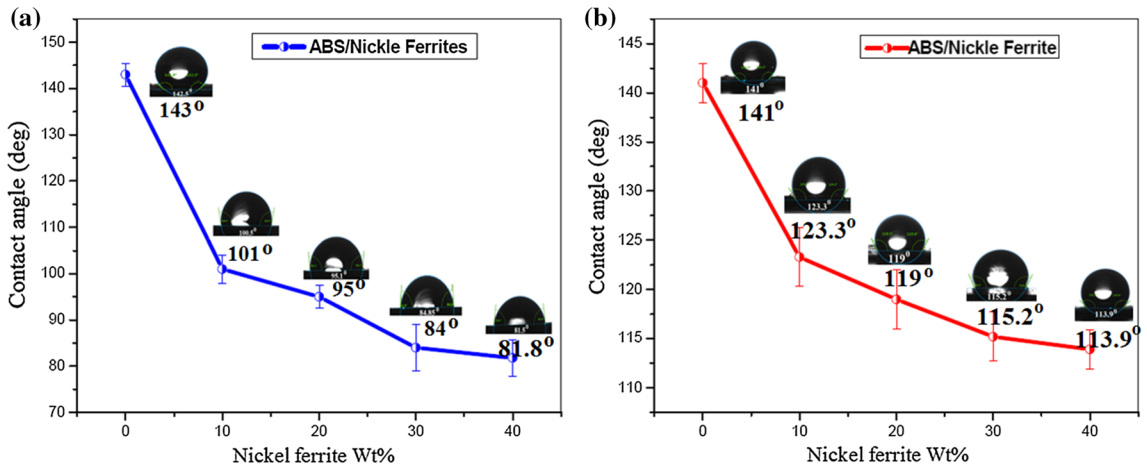


Fig. 12. Thin film contact angle characteristics of various $NiFe_2O_4$ weight fractions. (a) Solution casted thin films, and (b) LVHPAA spray coated thin films.

leakage current and potential discharge under heavily contaminated conditions additionally lowering the electrostatic arcing effect.[78] Furthermore, over in past decades microwave, integrated circuit improvements have been achieved by increasing transistor speed, reducing its size and advancements of integrating components in single chip packaging technologies. Wherein, miniaturization of electronic components can operate faster, so integrated circuits have become faster. However, integration of elements in a single chip is more complicated, an emerging factor being that, integration may disrupt the signal propagation within the chips, signal delays were caused by shorting or interconnection, which has been increasing while reducing towards micro and nano with each generation of scaling and may soon limit the overall performance of the devices.[5,79] Such a type of functional electronic components may induce malfunctioning due to shortening, burning of insulation material by anodization under critical moisture conditions.[80] Therefore, in recent days researchers have been approaching towards intrinsically stimulated hydrophobic dielectric characteristics in materials, which are of vital interest to digital electronics and integrated circuits as well as other electronic components in miniaturizing single chip packaging technology.

The stable surface wettability is determined by interfacial adhesion and cohesion forces, where the deposited water droplet spreads over a horizontal thin film surface until their intrinsic molecular cohesion under the influenced gravitational force field conditions. If the water droplet influencing internal forces are balanced, which in turn causes an equilibrium state, then the contact angle measurements can be performed by the Contact Goniometer. Where the water droplet internal

force's equilibrium state influenced a gravitational force field tendency then it elucidates that the minimal energy state of three phases acting between the water surface and solid surface, which can be additionally demonstrated with the aid of Young's relation. The mathematical representation is $\gamma_{SG} = \gamma_{SG} + \gamma_{SG} * \cos\theta$. Where the '$\gamma$' is the surface tension representative coefficient of solid–gas (SG), solid–liquid (SL) and liquid–gas (LG) interfaces.[81] However, this relation can be compatible for smooth and homogeneous surfaces, but not for the rough surfaces, where the nanoscale roughness pattern personifying heterogeneous textured nanoneedles induces capillary actions over water droplets known as capillary forces produces counteractions to that of the gravitational force acting on the water body, hence accomplishing roughness determined by hydrophobic characteristics.[82,83] The nanoscale morphological roughness patterns can be delineated by topographical images, which were obtained with the aid of raster scanned noncontact tapping mode atomic force microscopy. The methodology for demonstrating the prognosis of hydrophobicity on the nanoscale rough surface patterns from 2-D and the 3-D images is illustrated in Fig. 10a and b. Wherein, the morphological surface roughness value increases while increasing nickel ferrite weight fractions were visually perceived. The AFM characteristic root mean square (RMS) results of as-fabricated thin films are shown in Fig. 11a and b (see supplementary Table S1). This elucidates that the noticeable transmutation of surface morphology is a direct path mechanism for hydrophobic to hydrophilic transition, which probably can be attributed to a hydrophilic oxide phase present in the nanocomposites. Additionally, 3-D micrographs suggest that the existence of sharp nanoneedles yields nanoscale roughness, this inherent nanoscale property conjugated with hydrophilic oxide phase intensifies their hydrophilic characteristics with increasing nickel ferrite weight fractions. Whereas, the role of the roughness parameter amplifies the contact angle measurements, which might be in either directions negative (decreases) or positive (increases) and consequently imports hydrophilic or hydrophobic features of the respective surface. Balasubramanian K et al., have reported that increases in surface roughness caused a super-hydrophobic nature for the coatings.[84] Moreover, P J V Zowl et al., have demonstrated roughness parametric value increases with increasing sharp needles with consequently capillary forces acting on the surfaces, but either of hydrophilicity or hydrophobicity that corresponds to their threshold percolation limit.[85] This probability facilitates the superior hydrophobic characteristics in the case of LVHPAA assisted ABS/nickel ferrite nanocomposites, and further which has imminent hydrophilic attributes while increasing nickel ferrite weight fractions.

The goniometric measurement is used to capture either hydrophilic or hydrophobic characteristic (contact angle) with the aid of combined Wenzel and Cassie Baxter mathematical models.[81,86,87] This significant contact angle measurement is precisely attributed to thin film's surface morphology and chemical composition. Wherein, the water droplet consisting of the 8 $\mu$l volume is injected onto the surface of fabricated nanocomposite thin films to estimate static water contact angle measurements. Whereas, the contact angle measurements elucidate that the incremental weight fractions diminish static water contact angle measurements, which probably can be attributed to heterogeneous surface roughness characteristics. The roughness analyzed contact angle measurements have been illustrated in Fig. 10a and b. Additionally, the water contact angle measurements with different wt.% nickel ferrites are shown in Fig. 12. Where the water contact angle readings 142.5°–81.8° were obtained from solvent casted thin film fabrication technique as well as the results 141°–130.9° were observed by LVHPAA spray assisted technique. However, the hydrophobic result obtained by the LVHPAA spray supported technique is superior to the solvent casting technique, which probably elucidates that the atomized nanoneedles induced homogeneous surface roughness characteristics, which controls an intensified hydrophobic to hydrophilic transition mechanism.[88] Therefore, from this study, it is demonstrated that the solvent caste thin films were approaching towards hydrophilic characteristics while increasing wt.% configurations. Whereas, the LVHPAA spray coated method facilitates exponentially decaying contact angular readings, where the spray atomized mechanism controls hydrophilic characteristics by introducing homogeneous textured nanoneedles on the surface instigates uniform capillary forces acting on the droplets. Hence, this superior hydrophobic characteristic facilitates an electronic counter mechanism against water droplets induced for mal-operation in miniaturized electronic technology, integrated circuits, in electronic packaging technologies and other electronic devices.

## CONCLUSION

ABS and $NiFe_2O_4$ amalgamated ABS polymer thin films were successfully fabricated with the aid of solution casted ($\sim$ 0.45 mm) and the LVHPAA spray coated ($\sim$ 0.45 mm) technique. The ABS polymer amorphous structure ($2\theta$ = 15°–25°) and nickel ferrite crystalline phases (JCPDS:00-010-0325) were elucidated by utilizing the x-ray diffraction spectroscopy. Additionally, the interconnected nickel ferrite infrared absorption bands (600–490 $cm^{-1}$) and ABS functional groups were examined by a FT-IR spectro-

meter. Moreover, the frequency ($10^1$–$10^7$ Hz) respective space charge polarization at lower frequencies was explained by the MWS polarization hypothesis. Subsequent higher frequency dielectric constant characteristics were elucidated with the aid of an oriental polarization mechanism, simultaneously oriental dipole resonance phenomena in thin films were observed, this illustrates patronizing exponential decay dielectric permittivity characteristics within the frequency range ($10^1$–$10^7$ Hz). Concurrently, thin film's nickel ferrite concentrations revealed dielectric permittivity $\sim$ 2.4–4.5 and $\sim$ 2.4–10.5 for casted and LVHPAA spray technique, which probably can be attributed to the conductivity and impedance characteristics. Furthermore, the effect of as-fabricated nanocomposite thin films quantitatively (LVHPAA: 141° to 113.9° and casted technique: 142.5° to 81.8°) hydrophobic textured surfaces were analyzed by combined AFM and contact goniometry. Where, the AFM nanoneedles induced a roughness factor that is a predominant parameter to produce hydrophobicity, which was (6.75–182.16 nm) for casted technique and (10.927–240.066 nm) for LVHPAA assisted fabrication technique. However, the demonstrated LVHPAA technique produces nanoparticle dispersion induced well EM interactions to quantify the superior dielectric characteristics concurrently with atomized surface nanoneedles influencing qualitative roughness factor to control the hydrophobic characteristics better than the solvent casted technique. Therefore, it is envisioned that the utilization of the LVHPAA thin film's admirable technique renders the superior dielectric and hydrophobic characteristics by varying wt.% nickel ferrites, and it offers a rapid, convenient route to produce nanocomposite thin films.

### Associated Content

Supplementary information: Solvent casted and LVHPAA spray coated techniques administered nanocomposites demonstrated interfacial properties such as dielectric permittivity and contact angle hydrophobicity with uniform thickness is represented in Table S1, and their correlative investigations elucidate that the nanocomposites fabricated by low volume high-pressure air atomized technique exhibited superior characteristics than did the solvent casted fabrication technique. The Table S2, reveals the JCPDS reference No. 00-010-0325 and the Table S3, reveals a thin film's bond analysis—various stretching modes obtained in FT-IR spectra.

## ACKNOWLEDGEMENTS

The authors sincerely acknowledge Dr. Hina Gokhale, Vice Chancellor, DRDO-DIAT (DU) for motivation and support. Authors would like to thank Dr. Surendra K. Pal, Former Vice Chancellor, DIAT (DU), for the encouragement and support. The authors would also like to acknowledge Dr. S. R. Vadera, Director of Defence Laboratory, Jodhpur for continuous help and support.

## ELECTRONIC SUPPLEMENTARY MATERIAL

The online version of this article (https://doi.org/10.1007/s11664-018-6452-x) contains supplementary material, which is available to authorized users.

## REFERENCES

1. R.R. Tummala, P. Chahal, and S. Bhattacharya, in *IMAPS 35th Nordic Conference*, Sweden (1998).
2. Yang Rao and C.P. Wong, *J. Appl. Polym. Sci.* 92, 4 (2004).
3. U.R. Kevin and L.W. Schaper, *Integrated Passive Component Technology* (Piscataway: IEEE press, 2003), p. 381.
4. J. Hao, Y. Wei, and J. Mu, *RSC Adv.* 90, 87433 (2016).
5. S. Denis, T. Abell, F. Iacopi, and K. Maex, *Mater. Today* 1, 34 (2004).
6. C. Feger, *Polymeric Materials for Electronics Packaging and Interconnection*, ed. J.H. Lupinski and R.S. Moore (Washington: American Chemical Society, 1989), p. 407.
7. L.J. James and L.A. Hughes, *Handbook of polymer coatings for electronics: chemistry, technology and applications*, 2nd ed. (New York: Noyes Publications, 1990).
8. J.W. Balde, Overview of multichip technology, (Electronic Materials Handbook 1 1982).
9. K. Xie, S.Y. Zhang, J.G. Liu, M.H. He, and S.Y. Yang, *J. Polym. Sci., Part A: Polym. Chem.* 15, 2581 (2001).
10. L.A. Ramajo, A.A. Cristóbal, P.M. Botta, J.P. López, M.M. Reboredo, and M.S. Castro, *Compos. A Appl. Sci. Manuf.* 40, 388 (2009).
11. D. Kuo, C.C. Hau, TYSu Chang, W.K. Wang, and Y. Lin, *J. Eur. Ceram. Soc.* 9, 1171 (2001).
12. D.M. DeLongchamp and P.T. Hammond, *Adv. Funct. Mater.* 14, 224 (2004).
13. H. Andreas, *Polymer Films with Embedded Metal Nanoparticles* (Berlin: Springer, 2013), pp. 1–199.
14. C.H. Liu and S.S. Fan, *Appl. Phys. Lett.* 86, 123106 (2005).
15. J.K. Nelson and Y. Hu, *J. Phys. D Appl. Phys.* 38, 213 (2005).
16. W. Haifeng, W. Cao, Q.F. Zhou, K.K. Shung, and Y.H. Huang, *Appl. Phys. Lett.* 85, 5998 (2004).
17. D. Vollath, D.V. Szabo, and S. Schlabach, *J. Nanopart. Res.* 6, 181 (2004).
18. AYu Barnakov, B.L. Scott, V. Golub, L. Kelly, V. Reddy, and K.L. Stokes, *J. Phys. Chem. Solids* 65, 1005 (2004).
19. K. Hilmar, G. Price, N.A. Pearce, M. Alexander, and R.A. Vaia, *Nat. Mater.* 3, 115 (2004).
20. J.L. Wilson, P. Poddar, N.A. Frey, H. Srikanth, K. Mohomed, J.P. Harmon, S. Kotha, and J. Wachsmuth, *J. Appl. Phys.* 95, 1439 (2004).
21. N. James and K. Pielichowski, *Adv. Eng. Mater.* 5, 769 (2003).
22. S. Shouheng, S. Anders, H.F. Hamann, J.U. Thiele, J.E.E. Baglin, T. Thomson, E.E. Fullerton, C.B. Murray, and B.D. Terris, *J. Am. Chem. Soc.* 124, 2884 (2002).
23. C. Jhunu, Y. Haik, and C.J. Chen, *J. Magn. Magn. Mater.* 246, 382 (2002).
24. M. Morihiko and Y. Miyata, *J. Appl. Phys.* 91, 9635 (2002).
25. A.A. Novakova, V. Yu Lanchinskaya, A.V. Volkov, T.S. Gendler, T. Yu Kiseleva, M.A. Moskvina, and S.B. Zezin, *J. Magn. Magn. Mater.* 258, 354 (2003).
26. Y. Özlem, M.K. Ram, M. Aldissi, P. Poddar, and S. Hariharan, *J. Mater. Chem.* 15, 810 (2005).
27. R.K. Kotnala, S. Ahmad, A.S. Ahmed, J. Shah, and A. Azam, *J. Appl. Phys.* 112, 054323 (2012).
28. G.R. Pulliam, *J. Appl. Phys.* 38, 1120 (1967).
29. I. Hideaki, T. Uemura, H. Yamaguchi, and S. Naka, *J. Mater. Sci.* 24, 3549 (1989).
30. A. Masanori and Y. Tamaura, *J. Appl. Phys.* 55, 2614 (1984).

31. W. Chen, W. Zhu, O.K. Tan, and X.F. Chen, *J. Appl. Phys.* 108, 034101 (2010).
32. T. Terumitsu, H. Kurisu, M. Matsuura, Y. Shimosato, S. Okada, K. Oshiro, H. Fujimori, and S. Yamamoto, *J. Appl. Phys.* 99, 08N507 (2006).
33. A. Raghunathan, I.C. Nlebedim, D.C. Jiles, and J.E. Snyder, *J. Appl. Phys.* 107, 09A516 (2010).
34. F.C. Krebs and C. Frederik, *Sol. Energy Mater. Sol. Cells* 93, 394 (2009).
35. M. Pedro, C.M. Costa, M. Benelmekki, G. Botelho, and S.L. Mendez, *CrysEngComm.* 14, 2807 (2012).
36. U. Siemann, *Progr. Colloid Polym. Sci.* 130, 1 (2005).
37. P. Martins, C.M. Costa, G. Botelho, M.S. Lanceros, J.M. Barandiaran, and Gutierrez, *J. Mater. Chem. Phys.* 8, 698 (2012).
38. J.R. Dutcher and A.G. Marangoni, *Soft Materials Structure and Dynamics* (New York: Mercel Dekker, 2005).
39. T.K. Manish, I.S. Bayer, G.M. Jursich, T.M. Schutzius, and C.M. Megaridis, *ACS Appl. Mater. Interfaces.* 2, 1114 (2010).
40. P.M. Gore, S. Zachariah, P. Gupta, and K. Balasubramanian, *RSC Adv.* 107, 105180 (2016).
41. B.S. Banerjee and K. Balasubramanian, *RSC Adv.* 5, 13653 (2015).
42. K.Y. Byung, V. Doojin, J. Jang, I.N. Seok, S.K. Seok, K.K. Mi, and Y.K. Dong, *IEEE J. Quantum Electron.* 16, 1838 (2010).
43. S.D. Sovani, P.E. Sojka, and A.H. Lefebvre, *Prog. Energy Combust. Sci.* 27, 483 (2001).
44. P. Vinay and K. Pal, *Compos. B Eng.* 46, 114 (2017).
45. O. Anil, K. Singh, A. Chandra, and S.K. Dhawan, *ACS Appl. Mater. Interfaces.* 2, 927 (2010).
46. D. Camille, R. Cueff, C. Aumeran, G. Garrait, B.M. Jensen, O. Traoré, and V. Sautou, *PLoS ONE* 10, e0135632 (2015).
47. N. Bhardwaj, K.S. Manjula, B. Srinivasulu, and S.C. Subhas, *Open J. Org. Polym. Mater.* 2, 75 (2012).
48. K. Rachida and I. Debah, *Mater. Sci. Appl.* 2, 404 (2011).
49. B.G. Jayesh and S. Schlick, *Polymer* 43, 3239 (2002).
50. R.M. Santos, G.L. Botelho, and A.V. Machado, *J. Appl. Polym. Sci.* 116, 2005 (2010).
51. S. Daniela, E. Pouyet, L. Toniolo, M. Cotte, and A. Nevin, *Anal. Chim. Acta* 843, 59 (2014).
52. L. Andre, A. Petit, and D. Bogdal, *Liquid–liquid PTC in which the inorganic anions or anionic species generated from relatively strong organic acids are located in the aqueous phase and react Microwai ts\n Organic Synthesis, Srumii edition I-dited by A. loupy* (Weinheim: WILEY-VCH Verlag GmbH & Co. KGaA, 2006), p. 278.
53. M. Willander, O. Nur, M.Q. Israr, A.B. Abou Hamad, F.G. El Desouky, M.A. Salem, and I.K. Battisha, *J. Crystal. Process Technol.* 2, 1 (2012).
54. T. Jitendra and K. Khushbu, Rahangdale, and K. Balasubramanian, RSC. *Advances.* 6, 69733 (2016).
55. T. Jitendra, K. Khushbu, R. Rahangdale, B.Kandasubramanian Aepuru, and S. Datar, *RSC Adv.* 6, 36588 (2016).
56. A.R. James, C. Prakash, and G. Prasad, *J. Phys. D Appl. Phys.* 39, 1635 (2006).
57. W. Rainer, *Nanoelectronics and information technology* (Hoboken: Wiley, 2012), p. 1031.
58. M. Karen, M.R. Baklanov, D. Shamiryan, F. Lacopi, S.H. Brongersma, and Z.S. Yanovitskaya, *J. Appl. Phys.* 93, 8793 (2003).
59. W.C. Chun, J.F. Song, H.M. Bao, Q.D. Shen, and C. Zheng, Yang. *Adv. Funct. Mater.* 18, 1299 (2008).
60. L. Peter, V. Bobnar, A.V. Pronin, A.I. Ritus, A.A. Volkov, and A. Loidl, *Phys. Rev. B* 66, 052105 (2002).
61. R.K. Kotnala, S. Ahmad, A.S. Ahmed, J. Shah, and A. Azam, *J. Appl. Phys.* 112, 054323 (2012).
62. K. Vasundhara, B.P. Mandal, and A.K. Tyagi, *RSC Adv.* 5, 8591 (2015).
63. M.A. Osipov and M.V. Gorkunov, *Phys. Rev. E* 92, 032501 (2015).
64. D. Jacques, *Thin Solid Films* 8, 69 (1971).
65. S.S.N. Bharadwaja and S.B. Krupanidhi, *Thin Solid Films* 391, 126 (2001).
66. L. Yong, X. Huang, Z. Hu, P. Jiang, S. Li, and T. Tanaka, *ACS Appl. Mater. Interfaces.* 3, 4396 (2011).
67. Y. Kobayashi, T. Tanase, T. Tabata, T. Miwa, and M. Konno, *J. Eur. Ceram. Soc.* 28, 117 (2008).
68. N. Sivakumar, A. Narayanasamy, N. Ponpandian, and G. Govindaraj, *J. Appl. Phys.* 101, 084116 (2007).
69. T. Hanai and K. Sekine, *Colloid Polym. Sci.* 264, 888 (1986).
70. K.K. Patankar, S.S. Joshi, and B.K. Chougule, *Phys. Lett. A* 346, 337 (2005).
71. B.K. Mujasam, F.A. Mir, M.S.A. El-sadek, M. Shahabuddin, and N. Ahmed, *J. Nanopart. Res.* 15, 2067 (2013).
72. N. Ortega, A. Kumar, P. Bhattacharya, S.B. Majumder, and R.S. Katiyar, *Phys. Rev. B* 77, 014111 (2008).
73. S.V. Drappel, G. Liebermann, R.P. Veregin, T.E. Enright, S.M. Silence, M.J. Duggan, and P.J. MacLeod, (inventors; Xerox Corporation.). United States patent US: 6,391, 509 (2002).
74. S.C. Derek and A.R. West, *J. Appl. Phys.* 66, 3850 (1989).
75. C. Cabuz, T. R. Ohnstein, and E. I. Cabuz, United States patent: US 5,822,170, (1998).
76. J.W. Jack, *Smart Mater. Struct.* 10, 1115 (2001).
77. I. Hidenori, F. Arai, and T. Fukuda, *IEEE/ASME Trans. Mechatron.* 1, 68 (1996).
78. H. Homma, T. Kuroyagi, K. Izumi, C.L. Mirley, J. Ronzello, and S.A. Boggs, *IEEE Trans. Dielectr. Electr. Insul.* 6, 370 (1999).
79. H. Zheng, Z. Yuanfu, Y. Suge, F. Long, D. Shougang, C. Shougang, and Y. Chunqing, *J. Semicond.* 36, 115002 (2015).
80. R. Mancke, *IEEE Trans. Compon. Hybrids Manuf. Technol.* 4, 492 (1981).
81. T.S. Chow, *J. Phys. Condens. Matter* 10, L445 (1998).
82. P. Gupta and K. Balasubramanian, *Mater. Focus* 6, 556 (2016).
83. B.N. Sahoo, K. Balasubramanian, and M. Sucheendran, *J. Phys. Chem. C* 119, 14201 (2015).
84. K. Neha and K. Balasubramanian, *RSC Adv.* 5, 4376 (2015).
85. P.J.V. Zwol, G. Palasantzas, and J.T.M.D. Hosson, *Phys. Rev. E* 78, 031606 (2008).
86. P.M. Gore and K. Balasubramanian, *J. Mater. Chem. A* 6, 7457 (2018).
87. P. Gupta and K. Balasubramanian, *ACS Appl. Mater. Interfaces* 9, 19102 (2017).
88. R. Yadav, S.Zachariah Rohit, and K. Balasubramanian, *Adv. Sci. Eng. Med.* 8, 181 (2016).